frontiers in Earth Science

ORIGINAL RESEARCH
published: 05 October 2021
doi: 10.3389/feart.2021.756369

Localized Enhancement of Infrared Radiation Temperature of Rock Compressively Sheared to Fracturing Sliding: Features and Significance

Xiangxin Liu[1,2]*, *Lixin Wu*[3,4]*, *Yanbo Zhang*[1] and *Wenfei Mao*[3,4]

[1]College of Mining Engineering, North China University of Science and Technology, Tangshan, China, [2]College of Resources and Civil Engineering, Northeastern University, Shenyang, China, [3]School of Geosciences and Info-Physics, Central South University, Changsha, China, [4]Lab of Geohazards Perception, Cognition and Predication, Central South University, Changsha, China

Previous experiments indicated that infrared radiation temperature (IRT) was applied in monitoring rock stress or rock mass fracturing, and abnormal IRT phenomena preceding rock failure or tectonic earthquakes were frequently reported. However, the characteristics of IRT changing with rock fracturing and frictional sliding are not clear, which leaves much uncertainties of location and pattern identification of stress-produced IRT. In this study, we investigated carefully the localized IRT enhancement of rock compressively sheared to fracturing and sliding (named as CSFS) with marble and granite specimens. Infrared thermogram and visible photos were synchronously observed in the process of rock CSFS experiment. We revealed that localized IRT enhancement was determined by local stress locking, sheared fracturing, and frictional sliding, and the relations between the K_{cv} of IRT and the shear force are almost linear in wave length 3.7–4.8 μm. In the process of rock CSFS, the detected ΔIRT which resulted from thermoelastic effect is 0.418 K, while the detected ΔIRT resulted from friction effect reaches up to 10.372 K, which is about 25 times to the former. This study is of potential values for infrared detection of rock mass failure in engineering scale and satellite remote sensing of the seismogenic process in the regional scale.

Keywords: remote sensing rock mechanics (RSRM), infrared radiation temperature, localized IRT enhancement, compressively shearing to fracturing and sliding (CSFS), seismogenic process

OPEN ACCESS

Edited by:
Faming Huang,
Nanchang University, China

Reviewed by:
Lu Zheng,
Fuzhou University, China
Chunlai Wang,
China University of Mining and Technology, Beijing, China
Zhilu Chang,
Nanchang University, China

***Correspondence:**
Lixin Wu
wulx66@csu.edu.cn
Xiangxin Liu
liuxiangxin9@163.com

Specialty section:
This article was submitted to Environmental Informatics and Remote Sensing, a section of the journal Frontiers in Earth Science

Received: *10 August 2021*
Accepted: *17 August 2021*
Published: *05 October 2021*

Citation:
Liu X, Wu L, Zhang Y and Mao W (2021) Localized Enhancement of Infrared Radiation Temperature of Rock Compressively Sheared to Fracturing Sliding: Features and Significance. Front. Earth Sci. 9:756369. doi: 10.3389/feart.2021.756369

HIGHLIGHTS:

1) Localized IRT enhancement of the rock specimen in the process of CSFS is determined by local stress locking, sheared fracturing, and frictional sliding.

2) The K_{cv} of IRT and shear force displays a linear relationship before and after the rock being compressively sheared to fracturing and frictional sliding.

3) In the process of rock CSFS, the detected IRT enhancement resulted from friction effect exceeded 10 K, being 25 times about that resulted from thermoelastic effect.

INTRODUCTION

Earthquake is one of the most unexpected and most serious natural disasters, which is mainly resulted from the local locking of crustal stress and the sudden fracturing of rock mass or tectonic faults (Liu et al., 2016; Huang et al., 2018). Since Gorny et al. (1988) observed thermal infrared radiation anomalies before some medium-to-strong earthquakes in Central Asia, satellite remote sensing has been applied, or tried to be used in earthquake monitoring and precursor analysis (Saraf et al., 2009; Piroddi et al., 2014; Bhardwaj et al., 2017). Although the geoscience community has devoted decades to study the mechanism of seismicity and to seek for methods to monitoring rock fracturing and seismogenic process (Freund, 2003; Scoville and Freund, 2021), reliable abnormity recognition from remote sensing signals and accurate precursor identification are still challenging problems in the world.

Referring to the pioneering work of Geng et al. (1992) and Wu et al. (2000) in remote sensing rock mechanics (RSRM), the IRT change of stressed rock was investigated by many scholars (Wu et al., 2006a, 2006b; Liu et al., 2006; Liu et al., 2018; 2021; Wang et al., 2016; Salami et al., 2017; Huang et al., 2018; Huang et al., 2021; Zhao et al., 2019; Zhou et al., 2019; Cao et al., 2020; Huang et al., 2021; Yang et al., 2021) and applied to explore the rock fracturing behavior and related abnormal phenomenon. Wu et al. (2006a, 2006b) discovered that strong IRT emerged at the moment of rock bursting, and the anomalies of IRT image could be used as a precursor of rock fracturing. Liu et al. (2006) indicated that the fracturing mode of loaded rock affects IRT variation greatly, and IRT features were related to loading conditions and failure modes. Liu et al. (2018) also studied IRT localized enhancement in the condition of water infiltration in mine tunnels, and revealed thermogram was greatly affected by rock moisture. Wang et al. (2016) discussed specific relationship between IRT and stress, Salami et al. (2017) and Zhao et al. (2019) revealed that IRT is localized enhancement on crack tips, and Yang et al. (2021) used IRT to investigate quantitatively crack initiation, propagation, and coalescence during rock fracturing. Zhou et al. (2019) indicated that the loading rate had some impacts on IR images, and Cao et al. (2020) proposed a quantitative index of energy dissipation with the IRT ratio to analyze and monitor rock failure and instability. Besides, Watson et al. (1975) used IRT images to identify the near-surface physical state of geologic materials, by using a quantitative theoretical model for geothermal mapping and thermal inertia mapping, and Schöpa et al. (2011) utilized IRT images to determine the vent locations by stress field modeling in a Vulcano island, Italy.

Being a universal physical parameter in the process of solid material loaded to fracturing, IRT is usually used for identifying unstable rock slope (Mineo et al., 2015) and geothermal basin (Heasler and Jaworowski, 2018). There are basically two mechanisms of IRT rise: 1) force-induced thermomechanical coupling effect (Harwood et al., 1991) and 2) friction thermal effect (Wu et al., 2004). Freund et al. (2006a, 2006b) discovered that rock positive charge (P-holes) could be activated by stress and stimulate also infrared emission on the rock surface. However, the characteristics and mechanisms of localized IRT enhancement related to rock stress and local fracturing are not carefully studied or clearly interpreted.

In this study, compressively sheared to fracturing and sliding (CSFS) experiments on marble and granite specimens are conducted. IRT-localized enhancements captured by an infrared image are carefully studied both in time and space aspects. The relation between IRT enhancement and shear force is revealed, and the mechanisms of localized IRT enhancement are discussed.

EXPERIMENT METHODOLOGY

Preparation of Rock Specimens

Homogeneous marble and granite are selected to make rock specimens to avoid the anisotropic influence of mineral particles of different compositions and varied sizes. The uniform size of the specimens is 150 mm × 150 mm × 150 mm. The marble and granite specimens are labeled from "MHS-1" to "MHS-7" and "GSD-1" to "GSD-7," respectively. The marble specimen's mineral compositions include dolomite (60–65%), tremolite (25–30%), and calcite (5–8%). The granite specimen is an intrusive and egg-white rock with fine grains and a micrographic texture, and contains plagioclase (35–50%), potash feldspar (25–30%), quartz (20–25%), hornblende (3–5%), and biotite (2–5%).

The specimen is of glassy luster from mineral grains such as hornblende, quartz, and biotite, which are capable of inhomogeneous specular reflection. To prevent the uncertain impact of inhomogeneous specular reflection on IRT images, the specimen surface to be IRT imaged was painted evenly with black ink and then doted randomly with white chalk beforehand, which assisted in achieving a homogenous infrared reflection background, enhance the optical visibility, and improved the local identification of shear fracturing (**Figure 1A**). Validation test shows that the black ink and chalk dots have no negative impact on IRT detection (**Figure 1B**).

Boundary Conditions

The boundary conditions of tested rock specimens are shown in **Figure 2**. The shearing plane is the place where sheared fracturing and frictional sliding will happen. The active loading boundaries are composed of a normal force boundary at the up side and a shear loading boundary at the upper left side; oppositely, both the down side and lower right side act as passive loading boundaries. With both the upper right side and lower left side remaining free, the shear loading boundary provides horizontal load as shearing force, while the normal force boundary provides vertical load as normal stress.

Laboratory Equipment

The experimental system (**Figure 3**) comprises a loading system (RLW-3000, China), an infrared imaging system (InfraTec 8,325, Germany), and a CCD camera (Pike F-421, Germany). The setup of the laboratory equipment should be consistent to guarantee the

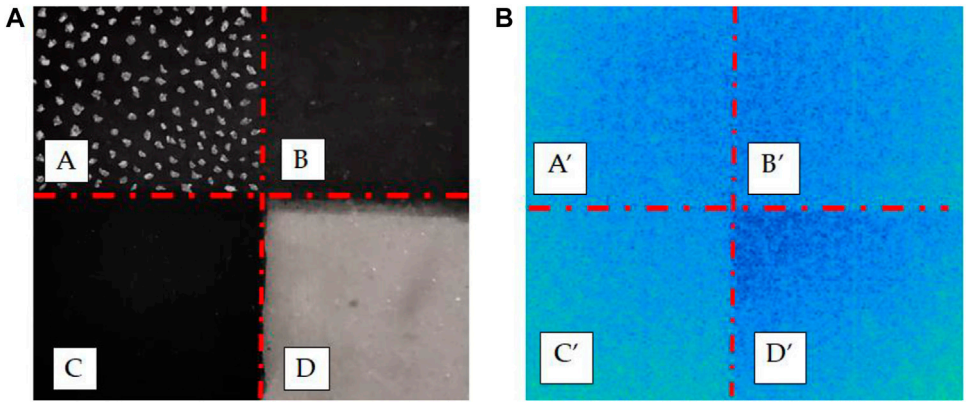

FIGURE 1 | Validation of IRT imaging **(A)** on rock surface whose four quarters are differently treated **(B)**. (A: thin ink painted and random chalk doted. A': IRT image of A; B: thin ink painted. B': IRT image of B; C: heavy ink painted. C': IRT image of C; D: original. D': IRT image of D).

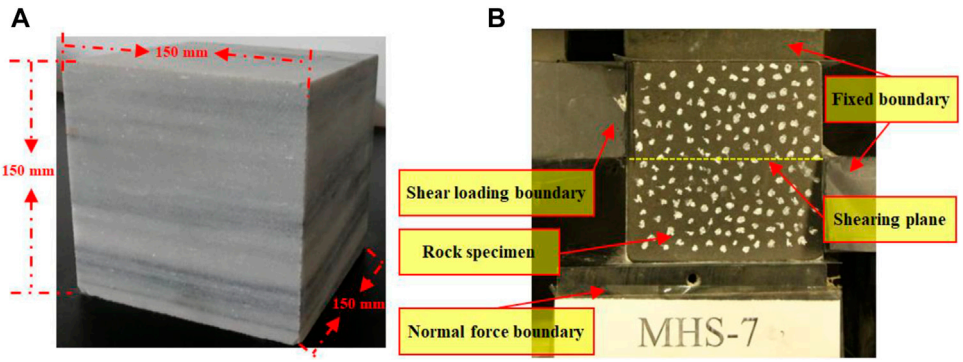

FIGURE 2 | Rock specimen and its boundary conditions for IRT imaging test in the process of CSFS experiment. **(A)** Back view of original specimen; **(B)**, front view of sheared specimen).

conformity of experiment data of different rock specimens (Ishida et al., 2017). The various components of the whole systems are set as follows:

1) Loading system: The vertical moving of loader along the axial direction is set as force control, and the loading rate is set as 1 kN/s. The horizontal moving of loader along shear direction is controlled by displacements, and the moving rate is set as 0.15 mm/min.
2) Infrared imaging system: The spectral range is 3.7–4.8 μm. The spatial resolution and sampling rate of the infrared monitoring system are set as 640 pixels × 512 pixels and 80 P/s, respectively. The accuracy of IRT measurement is set as ±0.1 *K*.
3) CCD camera: The spatial resolution and the sampling rate of CCD camera are set as 640 pixels × 512 pixels and 80 P/s, respectively.

The spectral range of 3–5 μm, named usually as intermediate infrared, is sensitive to be applied detecting the brightness temperature variation of objects with normal to high physical temperature. The detecting spectral range of the infrared imaging system, InfraTec 8,325, is 3.7–4.8 μm, which falls in the range of intermediate infrared, is good for detecting the IR enhancement in the process of rock loaded to fracturing.

Room temperature is controlled at 25°C approximately by an air conditioner, with temperature fluctuation being ±0.5 *K*. Light-blocking curtains are used to cover the laboratory windows to block sunshine and to prevent solar disturbance from outside in daytime. Furthermore, to reduce the disturbance of environmental radiation from walls and objects in the laboratory, several paper boards are set aside the rock specimen on the back, right, and left, leaving only the front side open to the infrared imaging system, as in **Figure 3**.

Data Analysis

Three indicators representing the variation of IRT, being *AIRT*, σ_{sd}, and K_{CV} of IRT, are selected for data analysis. *AIRT* is the average IRT of all the pixels inside a selected area and reflects the global or local energy input of mechanical force and the energy dissipation in the manner of infrared radiation (Wu et al., 2006a; 2006b). σ_{sd} reflects the absolute discrete degree of IRT inside the

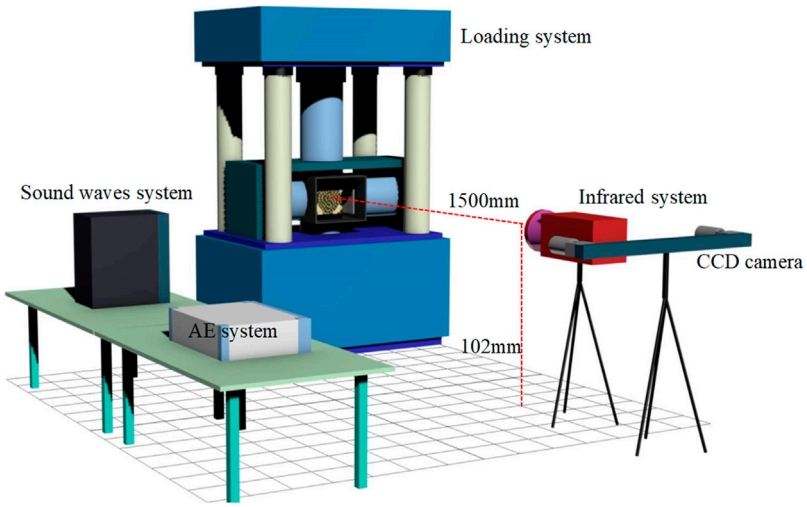

FIGURE 3 | Photos of experiment system in UCUST laboratory.

selected area of an IR image. K_{CV} is a relative value used to represent the discrete level of IRT inside the selected area. The computations of these indicators are as following:

$$AIRT = \frac{\sum_{i=1,j=m}^{m,n} \begin{bmatrix} IRT_{1\times1} & \cdots & IRT_{1\times n} \\ \vdots & \ddots & \vdots \\ IRT_{m\times1} & \cdots & IRT_{m\times n} \end{bmatrix}}{m \times n}, \quad (1)$$

$$\sigma_{sd} = \sqrt{\frac{1}{m \times n} \sum_{i=1,j=m}^{m,n} \left(IRT_{i\times j} - AIRT\right)^2}, \quad (2)$$

$$K_{CV} = \frac{\sigma_{sd}}{AIRT}. \quad (3)$$

RESULTS

The Process of Rock Fracturing

Normal force and shear force are applied gradually with a preset rate to reach the sheared fracturing and frictional sliding. The process of CSFS of a rock specimen is depicted in **Figure 4** with some typical moments in time sequence.

In the initial state (0s, **Figure 4A**), the rock specimen displayed homogeneous visible picture and infrared thermogram without structured differentiation; at 747.17s (**Figure 4B**), the visible picture displayed a small crack (V1), corresponding to T1 differentiation in thermogram; at 1,106.10s (**Figure 4C**), the visible picture appeared two cracks with V2 developing to be the shearing plane across the specimen and V3 occurred to the left end of the specimen, corresponding to T2 and T3 differentiations in thermogram. Besides, thermogram also exhibited two points (P1) of high IRT to the left end of the shearing plane along T2. At 1819.74s (**Figure 4D**), the visible picture displayed some fragment ejections (V6) corresponding to two low IRT zones (T6) occurred in thermogram, while several localized IRT enhancement points (P2) occurred notably along T2, which shows the undergoing compressive sliding behavior clearly.

Relationship Between Infrared Radiation Temperature and Shear Force

The relationship between IRT and shear force is beneficial to investigate IRT enhancement in the CSFS process. Accordingly, during the loading process, K_{cv} of IRT also exhibits approximate variation as shear force. As in **Figure 5** with marble specimen MHS-1 and granite specimen GSD-1 being examples, the mechanical process is divided into three stages, compressively loaded (stage I), compressively shearing loaded (stage II), and frictional sliding process (stage III).

1) Stage I, compressively loaded: the shear force of both marble and granite specimens kept an initial value, and the K_{cv} curves of IRT manifest a small fluctuation.
2) Stage II, compressively shearing loaded: K_{cv} and shear force increase at an accelerating rate with the constantly moving loader. The shear force curve of MHS-1 is slightly concaved, hinting a plastic deformation happens, while the shear force curve of GSD-1 is almost linear, hinting the elastic deformation happens and the granite is brittle.
3) Stage III, frictional sliding process: the curves of K_{cv} and shear force change differently, both manifesting an uncertain variation. However, the curves of MHS-1 are more complex than those of GSD-1, for example, the alternate rising and falling in MHS-1 (**Figure 5A**), and the up and phase step-up in GSD-1 (**Figure 5B**).

Furthermore, the shear force curves also include a transition point of stress change, such as T_M of specimen MHS-1 (**Figure 5A**) and T_G of specimen GSD-1 (**Figure 5B**), where

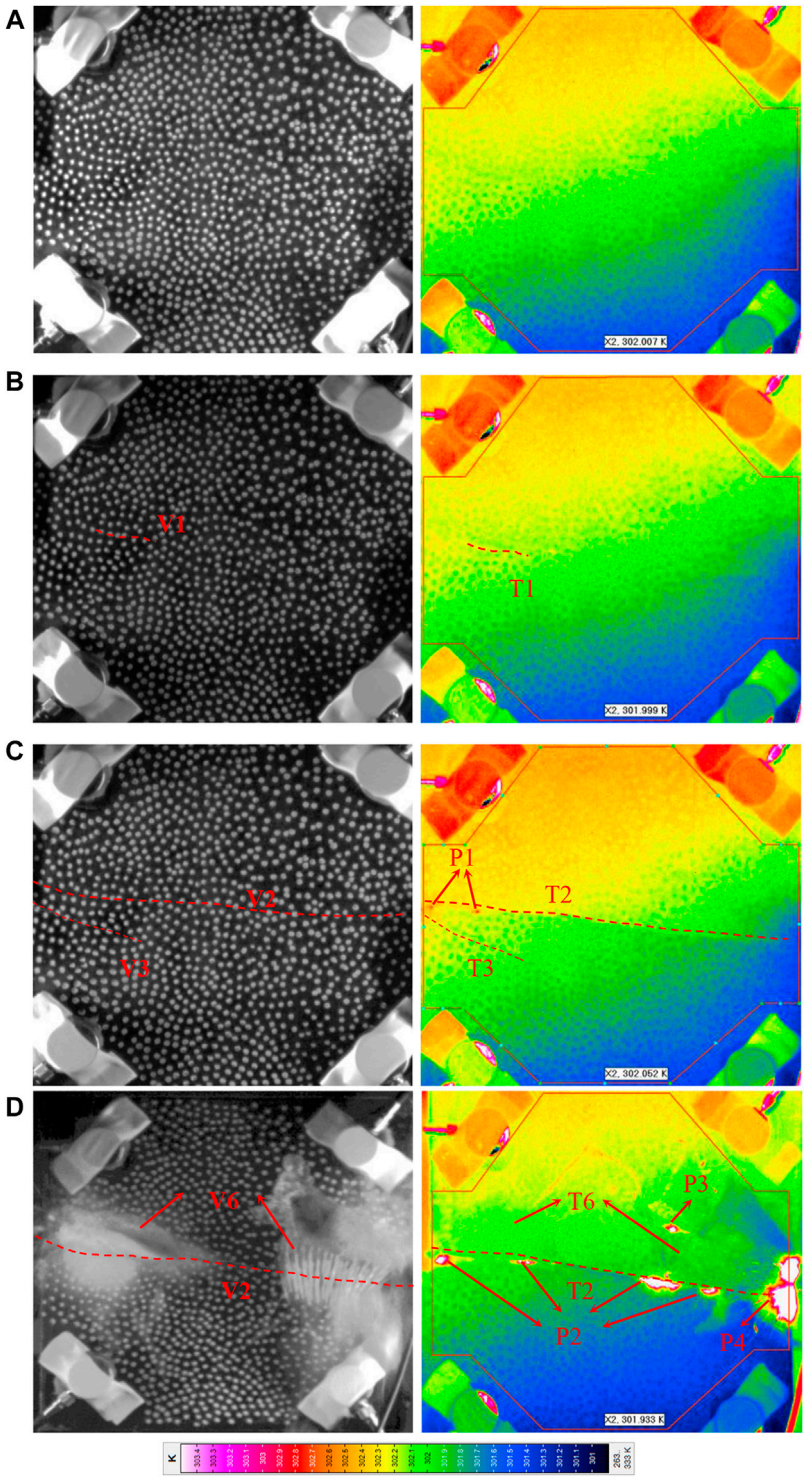

FIGURE 4 | Visible pictures **(left)** and infrared thermogram **(right)** of the fracturing process of GSD-1 specimen in the CSFS process. (a) 0s; b) 747.17s; c) 1,106.10s; d) 1819.74s. V and T denote fracturing lines in visible and infrared, respectively, and P denotes fracturing points with localized IRT enhancement).

the elastic phase and yield phase can be distinguished. The $K_{cv} - t$ curves manifest monotonic linear rise at the elastic phase, and transform into a complex changing at the yield phase.

Previous studies on the changes of IRT and rock stress had confirmed the linear relations between IRT and uniaxial compressive stress (Wu et al., 2006c; Xu et al., 2015). Here,

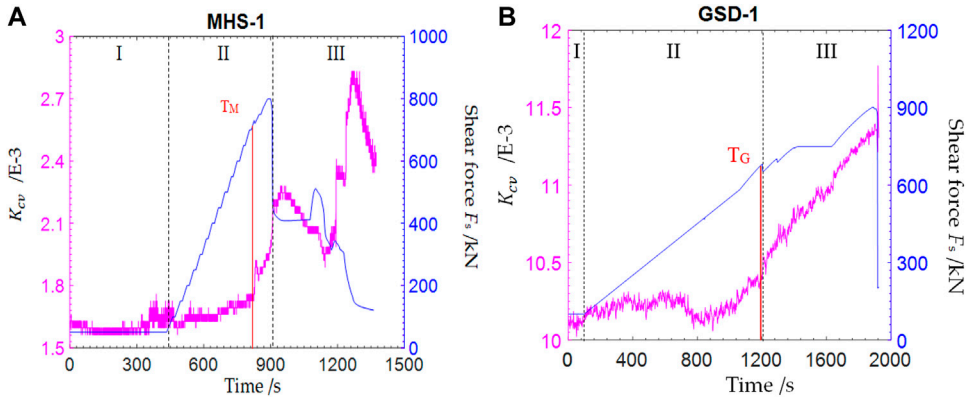

FIGURE 5 | Variation of shear force F_s and IRT K_{cv} with time during CSFS experiments. (a, MHS-1, b, GSD-1; I: compressively loaded; II: compressively shearing loaded; III: frictional sliding process).

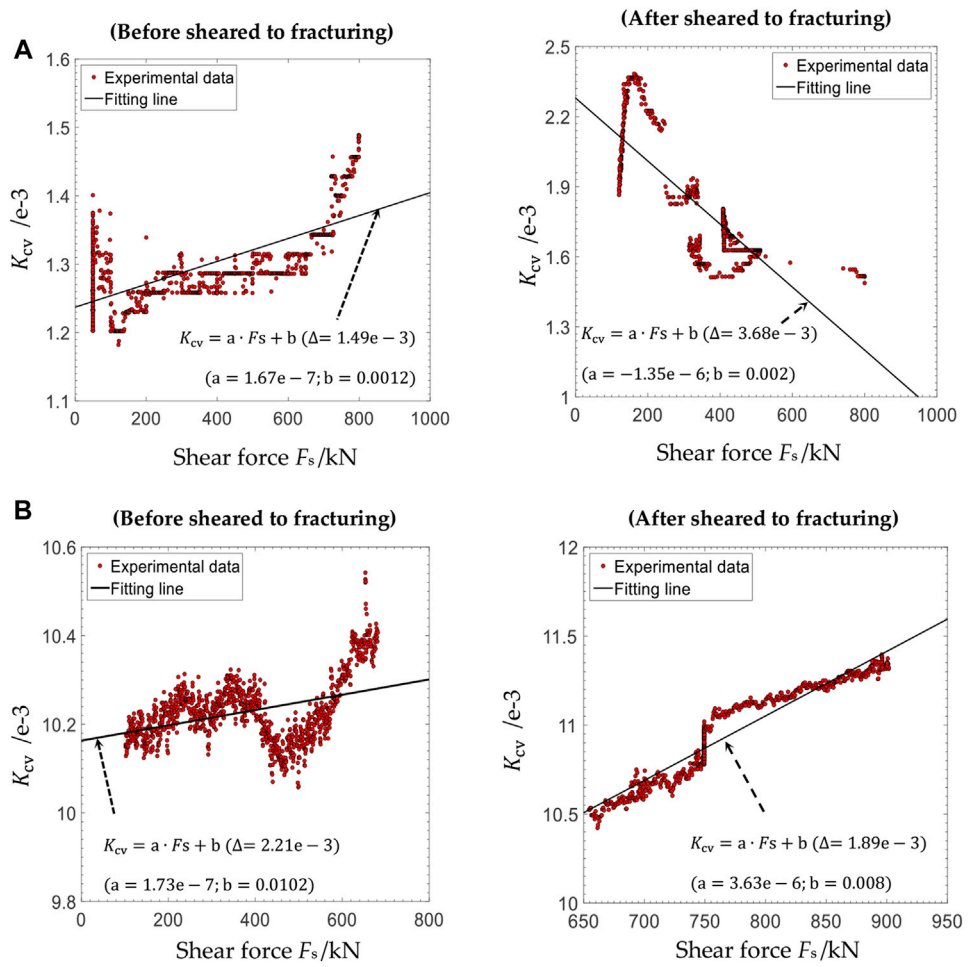

FIGURE 6 | Change of IRT K_{cv} with shear force F_s before and after sheared to fracturing. (a, MHS-1; b, GSD-1).

the distribution of fitting lines and the data points of IRT K_{cv} and shear force of MHS-1 and GSD-1 are shown in **Figure 6**. It shows that the relations between IRT K_{cv} and shear force of MHS-1 and GSD-1 before being sheared to fracturing are similar in a rising trend, while the relations between IRT K_{cv} and shear force of MHS-1 and GSD-1 after sheared to fracturing are different. The

TABLE 1 | Statistical information of shear force F_s and K_{cv}.

Lithology	Serial number	Before sheared to fracturing			After sheared to fracturing		
		$y = ax + b$[a]			$y = ax + b$[a]		
		a[a]	b[a]	Δ[b]	a[a]	b[a]	Δ[b]
Marble	MHS-1	1.67e–7	0.012	1.49e–3	–1.35e–6	0.002	3.68e–3
	MHS-2	4.16e–7	0.0013	3.21e–4	2.92e–7	0.0008	2.41e–3
	MHS-3	3.44e–8	0.0001	1.74e–4	2.67e–7	0.00015	7.22e–4
	MHS-4	1.77e–7	0.0015	9.61e–4	–1.25e–7	0.0019	6.29e–3
	MHS-5	1.49e–7	0.0012	6.82e–4	6.86e–7	0.0015	7.24e–3
Granite	GSD-1	1.73e–7	0.010	2.21e–3	3.63e–6	0.008	1.89e–3
	GSD-2	5.43e–7	0.010	2.01e–3	1.14e–6	0.009	8.31e–4
	GSD-3	–4.80e–8	0.0005	1.40e–3	–1.82e–7	0.0008	5.04e–4
	GSD-4	9.73e–8	0.0004	4.31e–4	2.81e–7	0.0003	2.10e–4
	GSD-5	2.23e–8	0.0012	5.67e–4	1.22e–7	0.0009	1.79e–3

[a]*y = ax + b is the regression model, where* a *is the slope value and* b *is the intercept value.*
[b]*Δ is the maximum residual modulus value.*

difference should be owing to the mechanical properties of marble with plastic deformation and granite with brittle fracturing. The correlation between IRT and shear force F_s before being sheared to fracturing and after being sheared to fracturing is represented by a regression model $y = ax + b$. The maximum residual modulus during the process before being sheared to fracturing is $\Delta \in [9.61e-4,\ 2.21e-3]$, and that during the process after being sheared to fracturing is $\Delta \in [8.31e-4,\ 7.24e-3]$. IRT change and stress variation are highly correlated, and the fitting effect of K_{cv} and F_s is ideal, which indicates that IRT is closely related with shearing stress.

The statistical results of all marble and granite specimens are shown in **Table 1**.

Localized Infrared Radiation Temperature Enhancement

In this study, the IRT enhancement, ΔIRT, is computed as follows:

$$\Delta IRT = IRT_i - IRT_{\mathrm{R}}, \tag{4}$$

where i represents the zone of lifted shear stress, IRT_i means the value of IRT in zone i, and IRT_{R} is the global value of IRT in a standard reference zone with shear stress unchanged.

$$\xi = \frac{\Delta T}{T_{\mathrm{R}}} \times 100\%, \tag{5}$$

where ξ represents the ratio of localized IRT enhancement in zone i.

1) Localized IRT enhancement from thermoelastic effect

As for MHS-1 in period 1,237.91s–1373.04s, the core zone of sheared fracturing increased significantly and experienced shearing stress accumulating, local locking, and delocking in sequence (**Figure 7**). Zone C is the stress locking region, and zone R is applied as a reference region. The IRT data obtained from the thermogram, as in **Figure 7**, are statistically shown in **Table 2**. The maximum IR enhancement occurred in the stress locking state, the value of IR enhancement is $\Delta T = 0.418\ K$, and the changing ratio ξ is up to +0.136%.

2) Localized IRT enhancement from friction sliding

Different kinds of stress or fracturing states (**Figures 8**–**10**) have different IRT localized enhancement forms (**Table 3**), for example, the pre-cracking zones on crack tip have a point-like form (X in **Figure 8**), the shear fracturing zones are in the form of continuous flecks (P1, P2, and P3 in **Figure 9**), and the sliding friction zones are ribbon-like (P1, P2, P3, P4, and P5 in **Figure 10**). The maximum IR enhancement appears at the moment of sliding fracturing; when ΔT is up to 10.372*K*, ξ is 3.441%.

In **Figures 9**, **10**, the mechanisms of IRT localized enhancements in shearing plane all belong to the friction effect, including frictional heat production (Wu et al., 2004) and emissivity lift (Wu et al., 2018). "L" is the time of local stress focus, and then intergranular dislocation is generated. The mechanism of IRT localized enhancement belongs to frictional heat production; "M" is the time of local stress concentration, and then macroscopic cracks are found. The mechanism of IRT localized enhancement is the friction effect; it includes T_{d} increased by frictional heat production and emissivity lift by surface fracturing and grinding behavior; "R" is the time of stress relaxation status, and local stress focus does not exist. The mechanism of IRT localized enhancement is only emissivity lift.

Therefore, the IRT enhancement mechanism and its proportion are calculated as in **Table 3**, for example, X1 in **Figure 8** and L in **Figures 9**, **10** only belong to frictional heat production, $FHP\% = 100\%$ and $EL\% = 0\%$; R in **Figures 9**, **10** only belong to emissivity lift, $FHP\% = 0\%$ and $EL\% = 100\%$; M in **Figures 9**, **10** have two mechanisms, its proportion on each mechanism calculates by **Eq. 6**, and **(7)** as follows:

$$FHP\% = \frac{\Delta T_M - \Delta T_R}{\Delta T_M}, \tag{6}$$

$$EL\% = 1 - FHP\% = 1 - \frac{\Delta T_M - \Delta T_R}{\Delta T_M} = \frac{\Delta T_R}{\Delta T_M}, \tag{7}$$

where ΔT_M is ΔT in M status; ΔT_R is ΔT in R status.

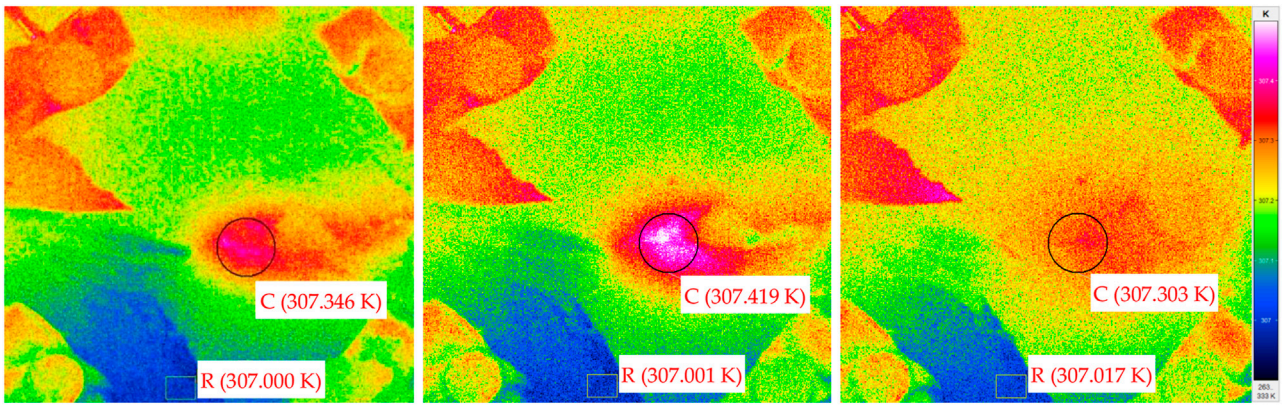

FIGURE 7 | Localized IRT enhancement of MHS-1 with stress change.

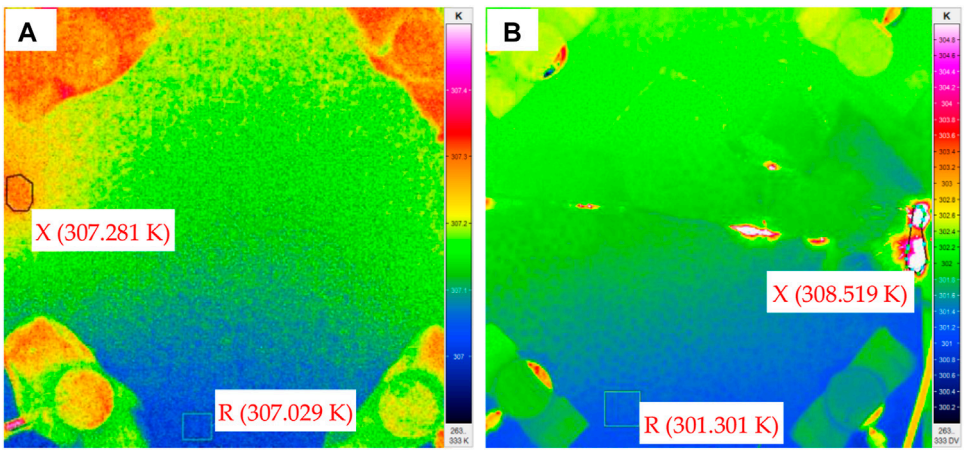

FIGURE 8 | Temperature increase caused by shear concentration. (a. MHS-1; b. GSD-1).

TABLE 2 | Statistical information of IRT localized enhancement by thermoelastic effect.

Stress accumulation in area C	T_C /K	T_R /K	ΔT /K	ξ /%
Stress accumulating (L in **Figure 7**)	307.346	307.000	0.346	0.113
Stress locking (M in **Figure 7**)	307.398	307.001	0.418	0.136
Stress relaxation (R in **Figure 7**)	307.302	307.303	0.286	0.093

DISCUSSION

Infrared Radiation Enhancement in the Process of Compressively Sheared to Fracturing and Sliding

According to infrared detection principles (Rees, 2001), the rock IRT, also called infrared brightness temperature as an index of infrared radiation energy detected by an infrared sensor with particular photoelectric system, is determined by both rock surface emissivity ε_λ and physical temperature T_d:

$$IRT = \sqrt[4]{\varepsilon_\lambda} \cdot T_d. \tag{8}$$

It illustrates that both the variation of emissivity ($\Delta\varepsilon_\lambda$) and the variation of physical temperature (ΔT_d) could change the detected IRT of rock specimen as follows:

$$\Delta IRT = \sqrt[4]{(\varepsilon_\lambda + \Delta\varepsilon_\lambda)}(T_d + \Delta T_d) - \sqrt[4]{\varepsilon_\lambda} \cdot T_d. \tag{9}$$

Accordingly, if ΔT_d is less than 0.5 K or could be ignored, ΔIRT is to be computed approximately as (Wu et al., 2018) follows:

$$\Delta IRT = IRT \times \left(\sqrt[4]{1 + \Delta\varepsilon_\lambda/\varepsilon_\lambda} - 1\right).$$

For example, if IRT = 300 K, ε_λ = 0.93, and $\Delta\varepsilon_\lambda$ = 0.03, the ΔIRT will be +2.4 K.

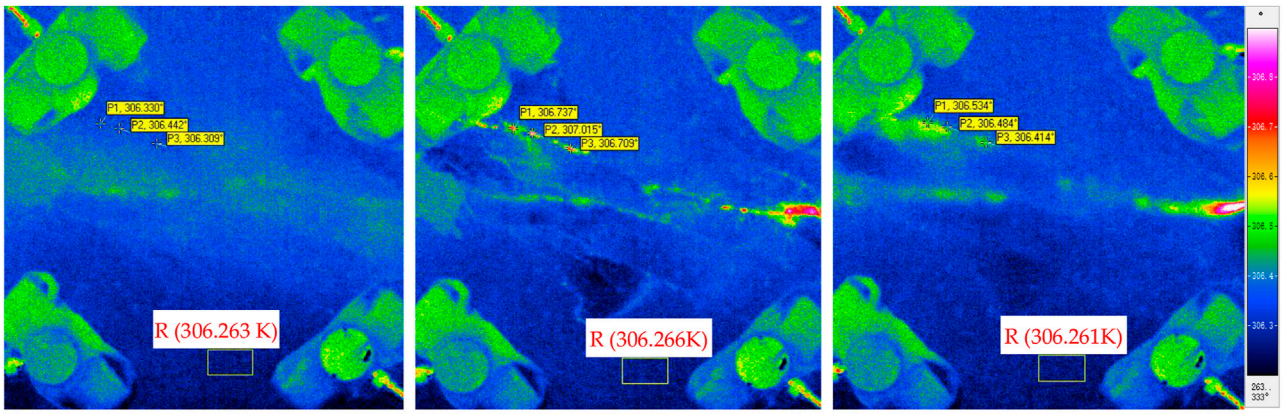

(L: before sliding; M: sliding moment; R: after sliding)

FIGURE 9 | IRT of MHS-4 related with a sliding action.

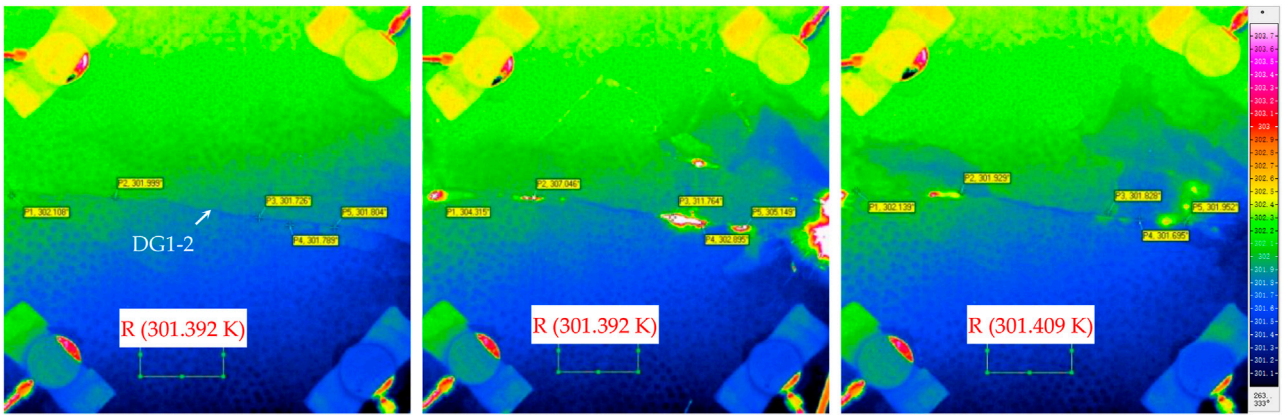

(L: before sliding; M: sliding moment; R: after sliding)

FIGURE 10 | IRT of GSD-1 related with a sliding action.

Since thermoelastic effect and friction thermal effect are able to cause local rise of T_d, and the surface fracturing and grinding behavior along shearing plane are able to cause local lift of ε_λ; all will contribute to localized IRT enhancement. There are many possibilities of T_d rise related with stress, that is, thermoelastic effect, friction thermal effect, and others such as phase transmission (**Figure 11**). Localized IRT enhancement will occur in some places if one or more than the above mechanisms get functioning in the process of CSFS. The dynamic change of rock surface IRT could be attributed to eight possible situations of stress that happened here and there: overall deformation increasing f_1, stress accumulating f_2, stress locking f_3, stress relaxation f_4, pre-cracking zone on crack tip f_5, shear fracturing zone f_6, sliding fraction zone f_7, and others f_8.

According to **Eq. 6**, the IR enhancement, ΔIRT, caused by ε_λ and T_d changes during the CSFS experiments, could be expressed as follows:

$$\Delta IRT = \begin{cases} f_1(\Delta T_d), & I \\ f_1(\Delta T_d) + f_2(\Delta T_d) + f_3(\Delta T_d) + f_4(\Delta T_d), & II \\ f_1(\Delta T_d) + f_2(\Delta T_d) + f_3(\Delta T_d) + f_4(\Delta T_d) & \\ \quad + f_5(\Delta T_d) + f_6(\Delta T_d) + f_7(\Delta T_d) + f_8(\Delta \varepsilon_\lambda), & III \end{cases}$$

where ΔT_d represents T_d change and $\Delta\varepsilon_\lambda$ is ε_λ change. I is the compressively loaded phase, II is the compressively shearing loaded phase, and III is the frictional sliding phase.

Significance of the Localized Infrared Radiation Enhancement

Localized IRT enhancement is related to the stress concentration phenomenon in space–time aspects, and the different enhancement mechanisms corresponds to different IR enhancement forms. Thermoelastic effect is often expressed as a regional type of IRT enhancement, for example, elliptic or circular type (C in **Figure 7**). Friction thermal effect is expressed as a point-like form (X in **Figure 8**), a

TABLE 3 | Statistical information of IRT localized enhancement by friction effect.

Stress or fracturing state		Area P	T_P /K	T_R /K	ΔT /K	ξ /%	IRT enhancement mechanism and its proportion/%	
							Frictional heat production (*FHP*)	Emissivity lift (*EL*)
Pre-cracking zone on crack tip (**Figure 8**)		X1 (**Figure 8A**)	307.281	307.029	0.252	0.082	100	
		X1 (**Figure 8B**)	308.519	301.301	7.218	2.400	100	
Shear fracturing zone (**Figure 9**)	Before (L in **Figure 9**)	P1	306.330	306.263	0.067	0.022	100	
		P2	306.442		0.179	0.058	100	
		P3	306.309		0.046	0.015	100	
	Moment (M in **Figure 9**)	P1	306.737	306.266	0.471	0.154	42.0	58.0
		P2	307.015		0.749	0.245	70.2	29.8
		P3	306.709		0.443	0.145	65.5	34.5
	After (R in **Figure 9**)	P1	306.534	306.261	0.273	0.089		100
		P2	306.484		0.223	0.073		100
		P3	306.414		0.153	0.050		100
Sliding friction zone (**Figure 10**)	Before (L in **Figure 10**)	P1	302.108	301.392	0.716	0.238	100	
		P2	301.999		0.607	0.201	100	
		P3	301.726		0.334	0.111	100	
		P4	301.789		0.397	0.132	100	
		P5	301.804		0.412	0.137	100	
	Moment (M in **Figure 10**)	P1	304.315	301.392	2.923	0.970	75.0	25.0
		P2	307.046		5.654	1.876	90.8	9.2
		P3	311.764		10.372	3.441	96.0	4.0
		P4	302.895		1.503	0.499	81.0	19.0
		P5	305.149		3.757	1.247	85.5	14.5
	After (R in **Figure 10**)	P1	302.139	301.409	0.730	0.242		100
		P2	301.929		0.520	0.173		100
		P3	301.828		0.419	0.139		100
		P4	301.695		0.286	0.095		100
		P5	301.952		0.543	0.180		100

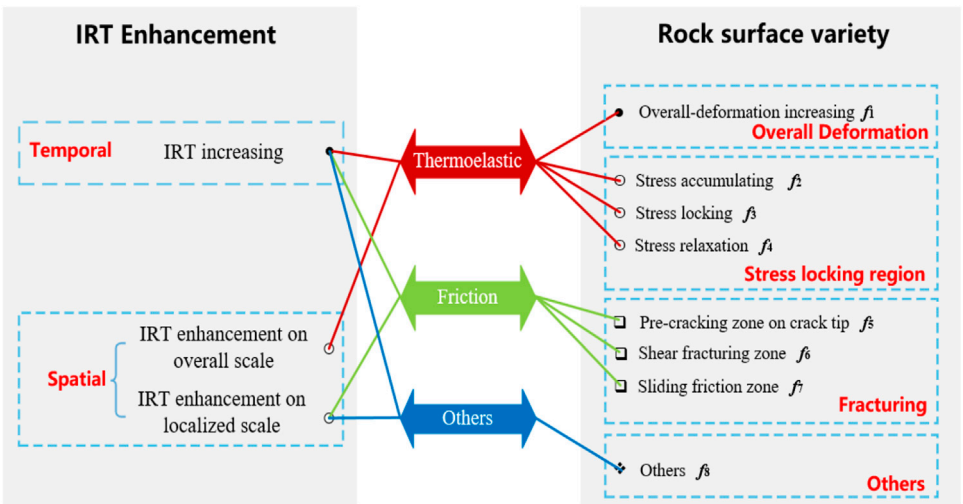

FIGURE 11 | Correlation between IRT changing and deformation or fracturing or stress distributions on rock surface during the CSFS process.

continuous fleck form (P1, P2, and P3 in **Figure 9**), or a ribbon-like form (P1, P2, P3, P4, and P5 in **Figure 10**) of IRT enhancement. In our research, ΔIRT caused by the thermoelastic effect is $0.418K$, and ΔIRT caused by the friction effect, which is a coupling of frictional heat production and emissivity lift, reaches up to $10.372K$.

Generally, an earthquake results from tectonic motion or crustal stress field alteration (Liao et al., 2003; Yohei et al., 2010), and the satellite infrared observation has been proven effective to monitor seismicity and the seismogenous process. The features of IR localized enhancement revealed in this study have at least two aspects relevant to satellite observation on crustal stress field alteration and the seismogenous process: 1) time aspect: K_{cv} of IRT represents the stress evolutions, and 2) space aspect: the location of localized IRT enhancement tells the place of stress concentration. Different types of localized IRT enhancement

correspond to different stress patterns, which could be identified from IRT monitoring, for instance, the area C of MHS-1 (**Figure 7**); areas P1, P2, and P3 of marble MHS-4 (**Figure 9**); and areas P1, P2, P3, P4, and P5 in granite GSD-1 (**Figure 10**).

Nevertheless, the localized IRT enhancement of a ground target would be affected by multiple environmental factors, such as sunlight reflecting, surface moisture, geoidal heights, viewing angle, and vegetation cover. Further experimental studies for different surface situations are demanded, even including different wavelength of electromagnetic wave for satellite observations. Detecting the infrared radiation anomaly related to earthquakes remains to be conquered due to multiple influencing factors. It is possible to extract the localized IR enhancement caused by crustal stress alteration from satellite observations, but it is especially challenging.

CONCLUSION

1) Localized IRT enhancement of rock specimen in the process of CSFS develops with stress variations, for example, a big bright spot reflects local stress locking, a point-like form and continuous flecks reflect the sheared fracturing, and a ribbon-like form reflects the frictional sliding.
2) The K_{cv} of IRT and shear force displays a linear relationship before and after the rock being compressively sheared to fracturing. There exists a close correspondence between IRT and stress in wave length 3.7–4.8 μm.
3) Different mechanisms lead to different IRT enhancement (ΔIRT) in quantity in the process of rock CSFS. By the thermoelastic effect, $\Delta IRT = 0.418\,K$ and $\xi = 0.136\%$, while by the friction effect, $\Delta IRT = 10.372\,K$ and $\xi = 3.441\%$, which is about 25 times to the former.

This experimental study provides new evidence and physical interpretation for imaging monitoring rock fracturing in the engineering scale and satellite remote sensing crustal stress field alteration in the regional scale with detection of infrared radiation brightness temperature. There are still some difficulties and challenges in the field of crustal stress monitoring by satellite infrared; further investigations are encouraged.

DATA AVAILABILITY STATEMENT

The raw data supporting the conclusions of this article will be made available by the authors, without undue reservation.

AUTHOR CONTRIBUTIONS

LX, WL, ZY, and MW participate in the test of compressively sheared to fracturing and sliding (CSFS).

FUNDING

This work was supported by the State Key Program of National Natural Science of China (No. 41930108) and the National Natural Science Foundation of China (Nos. 41977219 and. 51804122). All these are gratefully acknowledged.

REFERENCES

Bhardwaj, Anshuman., Singh, Shaktiman., Sam, Lydia., Bhardwaj, Akanksha., Martín-Torres, Javier., Singh, Atar., et al. (2017). MODIS-based Estimates of strong Snow Surface Temperature Anomaly Related to High Altitude Earthquakes of 2015. *Remote Sensing Environ.* 188, 1–8.

Cao, K., Ma, L., Wu, Y., Khan, N. M., and Yang, J. (2020). Using the Characteristics of Infrared Radiation during the Process of Strain Energy Evolution in Saturated Rock as a Precursor for Violent Failure. *Infrared Phys. Tech.* 109, 103406. doi:10.1016/j.infrared.2020.103406

Freund, F. T . (2003). Rocks that Crackle and Sparkle and Glow: Strange Pre-earthquake Phenomena. *J. Scientific Exploration* 17, 37–71.

Freund, F. T., Takeuchi, A., Lau, B. W. S., Al-Manaseer, A., Fu, C. C., Bryant, N. A., et al. (2006a). Stimulated Infrared Emission from Rocks: Assessing a Stress Indicator. *eEarth* 2 (1), 97–121. doi:10.5194/eed-1-97-2006

Freund, F. T., Takeuchi, A., and Lau, B. W. (2006b). Electric Currents Streaming Out of Stressed Igneous Rocks - A Step towards Understanding Pre-earthquake Low Frequency EM Emissions. *Phys. Chem. Earth* 31 (4/9), 389–396. doi:10.1016/j.pce.2006.02.027

Geng, N., Cui, C., and Deng, M. (1992). Remote Sensing Detection on Rock Fracturing experiment and the Beginning of Remote Sensing Rock Mechanics. *Acta Seismologica Sinica* 14, 645–652.

Gorny, V. I., Sal'Man, A. G., Tronin, A. A., and Shilin, B. V. (1988). Outgoing Infrared Radiation of the Earth as an Indicator of Seismic Activity. *Proc. Acad. Sci. USSR* 301, 5–7.

Harwood, N., Cummings, W. M., and MacKenzie, A. K. (1991). An Introduction in Thermoelastic Stress in: Thermoelastic Stress Analysis. *Adam Hilger* 1, 1–34.

Heasler, H., and Jaworowski, C. (2018). Hydrothermal Monitoring of norris Geyser basin, Yellowstone national park, USA, Using Airborne thermal Infrared Imagery. *Geothermics* 72, 24–46. doi:10.1016/j.geothermics.2017.10.016

Huang, J., Liu, S., Gao, X., Yang, Z., Ni, Q., and Wu, L. (2018). Experimental Study of the thermal Infrared Emissivity Variation of Loaded Rock and its Significance. *Remote Sensing* 10 (6), 818. doi:10.3390/rs10060818

Huang, J., Liu, S., Liu, W., Zhang, C., Li, S., Yu, M., et al. (2021). Experimental Study on the thermal Infrared Spectral Variation of Fractured Rock. *Remote Sensing* 13, 1191. doi:10.3390/rs13061191

Ishida, T., Labuz, J. F., Manthei, G., Meredith, P. G., Nasseri, M. H. B., Shin, K., et al. (2017). ISRM Suggested Method for Laboratory Acoustic Emission Monitoring. *Rock Mech. Rock Eng.* 50 (3), 665–674. doi:10.1007/s00603-016-1165-z

Liao, C., Zhang, C., Wu, M., Ma, Y., and Ou, M. (2003). Stress Change Near the Kunlun Fault before and after the Ms 8.1 Kunlun Earthquake. *Geophys. Res. Lett.* 30 (20), 2027. doi:10.1029/2003gl018106

Liu, S., Xu, Z., Wei, J., Huang, J., and Wu, L. (2016). Experimental Study on Microwave Radiation from Deforming and Fracturing Rock under Loading Outdoor. *IEEE Trans. Geosci. Remote Sensing* 54 (9), 1–10. doi:10.1109/tgrs.2016.2569419

Liu, S., Wu, L., and Wu, Y. (2006). Infrared Radiation of Rock at Failure. *Int. J. Rock Mech. Mining Sci.* 43 (6), 972–979. doi:10.1016/j.ijrmms.2005.12.009

Liu, X., Liang, Z., Zhang, Y., Liang, P., and Tian, B. (2018). Experimental Study on the Monitoring of Rockburst in Tunnels under Dry and Saturated Conditions Using AE and Infrared Monitoring. *Tunnelling Underground Space Tech.* 82, 517–528. doi:10.1016/j.tust.2018.08.011

Mineo, S., Pappalardo, G., Rapisarda, F., Cubito, A., and Di Maria, G. (2015). Integrated Geostructural, Seismic and Infrared Thermography Surveys for the Study of an Unstable Rock Slope in the Peloritani Chain (NE Sicily). *Eng. Geology* 195, 225–235. doi:10.1016/j.enggeo.2015.06.010

Piroddi, L., Ranieri, G., Freund, F., and Trogu, A. (2014). Geology, Tectonics and Topography Underlined by L'Aquila Earthquake TIR Precursors. *Geophys. J. Int.* 197 (3), 1532–1536. doi:10.1093/gji/ggu123

Salami, Y., Dano, C., and Hicher, P. Y. (2017). Infrared Thermography of Rock Fracture. *Géotechnique Lett.* 7 (1), 1–5. doi:10.1680/jgele.16.00131

Saraf, A. K., Rawat, V., Choudhury, S., Dasgupta, S., and Das, J. (2009). Advances in Understanding of the Mechanism for Generation of Earthquake thermal Precursors Detected by Satellites. *Int. J. Appl. Earth Observation Geoinformation* 11 (6), 373–379. doi:10.1016/j.jag.2009.07.003

Schöpa, A., Pantaleo, M., and Walter, T. R. (2011). Scale-dependent Location of Hydrothermal Vents: Stress Field Models and Infrared Field Observations on the Fossa Cone, Vulcano Island, Italy. *J. Volcanology Geothermal Res.* 203 (3), 133–145. doi:10.1016/j.jvolgeores.2011.03.008

Scoville, J., and Freund, F. T. (2021). Infrared Emission from Rocks in the Thermal Infrared (TIR) Window. *Eur. Phys. J. Spec. Top.* 230, 85–109. doi:10.1140/epjst/e2020-000246-4

Wang, C., Lu, Z., Liu, L., Chuai, X., and Lu, H. (2016). Predicting Points of the Infrared Precursor for limestone Failure under Uniaxial Compression. *Int. J. Rock Mech. Mining Sci.* 88 (10), 34–43. doi:10.1016/j.ijrmms.2016.07.004

Watson, K. (1975). Geologic Applications of thermal Infrared Images. *Proc. IEEE* 63 (1), 128–137. doi:10.1109/proc.1975.9712

Wu, L., Liu, S., Wu, Y., and Li, Y. (2004). Remote-sensing-rock Mechanics (IV) - Laws of thermal Infrared Radiation from Compressively-Sheared Fracturing of Rock and its Meanings for Earthquake Omens. *Chin. J. Rock Mech. Eng.* 23 (4), 539–544.

Wu, L., Mao, W., and Liu, S. (2018). Mechanisms of Altering Infrared-Microwave Radiation from Stressed Rock and Key Issues on Crust Stress Remote Sensing. *J. Remote Sensing* 22, 146–161.

Wu, L., Tang, C., and Zhong, S. (2006c). Comparison of thermal Infrared Radiation from Discontinuous Jointed Faults Fracturing with its Acoustic Emission and Stress Field. *Chin. J. Rock Mech. Eng.* 25 (6), 1111–1117.

Wu, L., Cui, C., Geng, N., and Wang, J. (2000). Remote Sensing Rock Mechanics (RSRM) and Associated Experimental Studies. *Int. J. Rock Mech. Mining Sci.* 37 (6), 879–888. doi:10.1016/s1365-1609(99)00066-0

Wu, L., Liu, S., Wu, Y., and Wang, C. (2006a). Precursors for Rock Fracturing and Failure-Part I: IRR Image Abnormalities. *Int. J. Rock Mech. Mining Sci.* 43 (3), 473–482. doi:10.1016/j.ijrmms.2005.09.002

Wu, L., Liu, S., Wu, Y., and Wang, C. (2006b). Precursors for Rock Fracturing and Failure-Part II: IRR T-Curve Abnormalities. *Int. J. Rock Mech. Mining Sci.* 43 (3), 483–493. doi:10.1016/j.ijrmms.2005.09.001

Xu, Z., Liu, S., and Wu, L. (2015). Comparative Study on the Variation Features of Infrared and Microwave Radiation in Deformation and Fracture Process of Rock. *J. Northeast. Univ. (Natural Science)* 36 (12), 1738–1742.

Yang, H., Liu, B., and Karekal, S. (2021). Experimental Investigation on Infrared Radiation Features of Fracturing Process in Jointed Rock under Concentrated Load. *Int. J. Rock Mech. Mining Sci.* 139, 104619. doi:10.1016/j.ijrmms.2021.104619

Yohei, Y., Yoshihisa, I., and Shigeki, H. (2010). Detailed Spatial Changes in the Stress Field of the 1984 Western Nagano Earthquake Region. *J. Geophys. Res. Solid Earth* 115 (B6), 1–17.

Zhao, D., Zhang, S., Zhao, Y., and Wang, M. (2019). Experimental Study on Damage Characteristics of Granite under Ultrasonic Vibration Load Based on Infrared Thermography. *Environ. Earth Sci.* 78 (14), 419. doi:10.1007/s12665-019-8450-6

Zhou, Z., Chang, Y., and Cai, X. (2019). Experimental Study of Infrared Radiation Effects of Rock with Different Loading Rates. *J. Cent. South Univ. (Science Technology)* 50 (5), 1127–1134.

Conflict of Interest: The authors declare that the research was conducted in the absence of any commercial or financial relationships that could be construed as a potential conflict of interest.

Publisher's Note: All claims expressed in this article are solely those of the authors and do not necessarily represent those of their affiliated organizations, or those of the publisher, the editors, and the reviewers. Any product that may be evaluated in this article, or claim that may be made by its manufacturer, is not guaranteed or endorsed by the publisher.